J. Fluid Mech. (1992), *vol.* 243, *pp.* 297–317
Printed in Great Britain

Satellite and subsatellite formation in capillary breakup

By M. TJAHJADI[1,3], H. A. STONE[2] AND J. M. OTTINO[1]

[1] Department of Chemical Engineering, Northwestern University, Evanston, IL 60208, USA
[2] Division of Applied Sciences, Harvard University, Cambridge, MA 02138, USA
[3] Current address: General Electric Company, Corporate Research and Development, Schenectady, NY 12301, USA

(Received 16 August 1991 and in revised form 16 January 1992)

An investigation of the interfacial-tension-driven fragmentation of a very long fluid filament in a quiescent viscous fluid is presented. Experiments covering almost three orders of magnitude in viscosity ratio reveal as many as 19 satellite droplets in between the largest droplets; complementary boundary-integral calculations are used to study numerically the evolution of the filament as a function of the viscosity ratio of the fluids and the initial wavenumber of the interface perturbation. Satellite drops are generated owing to multiple breakup sequences around the neck region of a highly deformed filament. In low-viscosity ratio systems, $p < O(0.1)$, the breakup mechanism is *self-repeating* in the sense that every pinch-off is always associated with the formation of a neck, the neck undergoes pinch-off, and the process repeats. In general the agreement between computations and experiments is excellent; both indicate that the initial wavenumber of the disturbance is important in the quantitative details of the generated drop size distributions. However, these details are insignificant when compared with the large variations produced in the drop size distributions owing to variation in the viscosity ratio.

1. Introduction

The study of breakup of fluid filaments is a classical problem in the fluid mechanics literature. Breakup leads to an array of uniformly spaced large droplets, referred to as mother drops, with smaller droplets in between, known as satellite drops. Typically, the dynamics are modelled as completely inviscid or are treated as a viscously dominated Stokes flow. The inviscid case can be traced back to Lord Rayleigh (1878) who studied the problem in the context of jet breakup and created a vast subsequent literature (Goedde & Yuen 1970; Bogy 1979; Chaudhary & Redekopp 1980; Chaudhary & Maxworthy 1980*a*, *b*; Mansour & Lundgren 1990). The viscous case can be traced to G. I. Taylor's studies of drop breakup in linear flows (Taylor 1934) and, more precisely, to his suggestion to study infinitely extended filaments in axisymmetric extensional flows, which was first investigated by Tomotika (1936) and subsequently studied in greater detail by Mikami, Cox & Mason (1975).

Theoretical analyses, based upon linear stability theory, highlight some of the most important interactions between flow and interfacial tension forces and can be used to predict the initial disturbance growth rate, the time for breakup, and the size of the mother drops. A linearized analysis, however, fails to capture the existence of satellite drops, which is a highly nonlinear phenomenon. Moreover, the analysis is also qualitatively incorrect in that breakup is assumed to occur at the midpoint between the two mother drops whereas, in fact, the midpoint is precisely the region where a large satellite forms.

Experimental counterparts are possible in both cases – jets and extended drops – but visualization is undoubtedly simpler in the case of viscous filaments as high speed photography is actually not necessary (e.g. Rumscheidt & Mason 1962). In fact, experiments involving visualization of extended viscous drops are relatively simple to perform. It is therefore surprising that a detailed study of the problem of satellite formation has remained unexplored. The main reason for the lack of detailed research is probably associated with the ability to stretch the drop significantly so as to approximate an infinite thread and the fact that this large stretching might not be possible in certain classes of flows. Thus, for example, most of the recent studies involving drop breakup have involved a four-roller device capable of generating a range of flows spanning from simple shear flow to planar extensional flow (Bentley & Leal (1986). However, in this apparatus, length stretches of more than 20 times the initial drop radius are difficult to achieve as the drop leaves the region where the flow is linear. Moreover, drops stretched 20 times the initial radius rarely behave as an infinite cylinder, as they are dominated by ends effects, and other modes of breakup (e.g. end pinching), rather than spatially-periodic capillary breakup, actually occur (Stone & Leal 1989).

Capillary breakup is common in a wide variety of mixing applications, and in particular, in stretching and dispersion in chaotic flows, the subject area which led us to undertake the present studies (Tjahjadi & Ottino 1991). Chaotic flows create exponential stretching and folding and overall length stretches of the order of 10^3, without noticeable breakup, are relatively easy to achieve. One such chaotic flow can be created by a time-periodic operation of two eccentric cylinders (Tjahjadi & Ottino 1991). Experimental studies in this flow reveal a wide distribution of stretching, widespread occurrence of capillary breakup, and a wide distribution of drop sizes generated upon breakup, with the drop size distribution typically covering up to three orders of magnitude or more. Also, long-time operation leads to statistically steady drop size distributions. Two regimes are possible: (i) repeated stretching and breakup – corresponding to the case of low viscosity ratios where drops stretch and break and the resulting fragments stretch and break again, until the fragments generated are too small to be noticeably affected by the viscous stresses, and (ii) one-time breakup, generally corresponding to viscosity ratios greater than one, where the filaments stretch and break but the fragments do not break again. Both situations, (i) and (ii), generate statistically invariant drop size distributions that can be collapsed in a single master curve for a wide range of viscosity ratios and operating conditions (Muzzio, Tjahjadi & Ottino 1991). Obviously, all drops, mother drops and satellites contribute to this distribution.

Whereas these findings are valuable in increasing our understanding of mixing, a more complete rationalization of the results rests on a detailed understanding of the process of breakup and satellite formation at the smallest scales. In this work we present an experimental and computational investigation of the time evolution and the details of the distribution of drop sizes generated upon breakup of highly extended fluid filaments in otherwise quiescent fluids.

The experiments involve stretching of drops in Couette flows, the initial conditions for breakup being achieved by stretching the drop under supercritical flow conditions. Effects of viscosity ratio and initial condition, i.e. wavelength of the initial perturbation, are examined. Fragmentation of the highly stretched filament into many satellite drops occurs after the flow is stopped. The computational results of filament fragmentation are carried out by means of boundary integral techniques for Stokes flows. Such techniques have been used in the past in a variety of problems involving free surfaces and appear to be ideally suited for the analysis of this type of problem. It should be pointed out that a boundary integral method for inviscid potential flow was used recently by Mansour & Lundgren (1990) in a study of jet breakup which also included a discussion of the formation of the first generation of satellite drops. In this work we consider the viscous dominated case; computations are compared with experimental results, and particular attention is given to the formation of several generations of satellite drops.

The most immediate application of the results obtained appears to be blending of polymer melts in mixing devices (Elemans 1989). The distribution of drop sizes is important in modelling transport processes and mechanical properties of blends. Thus, the distribution of drop sizes may affect rates of mass transfer between phases and interfacial chemical reactions. Also, transport properties such as gas permeability and mechanical properties of the processed material such as the elastic modulus are, in general, strongly dependent upon the morphology of the dispersion (Sax & Ottino 1975).

The paper is organized as follows: §2 summarizes the experiments and §3 briefly describes the numerical procedure; additional details regarding the numerical implementation are given in the Appendix. The results in §4 are divided into three parts: (§4.1) a typical breakup experiment that exhibits multiple pinch-offs, (§4.2) a comparison of the experimental observations with the results of the complementary numerical study, and (§4.3) investigation of the effects of viscosity ratio and initial wavenumber.

2. Experimental procedure

The experiments are performed in a Couette device. The apparatus consists of two concentric rotating borosilicate glass cylinders that can be rotated in the same or opposite directions. The diameter of the inner and outer cylinders are 99.7 and 131.0 mm, respectively. The suspending fluid is transparent corn syrup 1632 (Corn Products, Englewood Cliffs, NJ; viscosity about 326 poise at 23 °C). Effects of the bottom (lower) boundary are minimized by floating the suspending fluid on a denser and less viscous fluid (perfluoropolyether vacuum-pump oil or Fomblin® YL Vac 06/6, Aldrich). The drop fluid is a homogeneous mixture of no. 40 oil, an oxidized castor oil (CasChem Inc., Bayonne, NJ), and l-bromonaphthalene (Aldrich Chemical), predissolved with some organic dye (oil Blue N, or Oil Red N, Aldrich Chemical). Changing the volume fraction of l-bromonaphthalene allows the viscosity of the mixture to be varied from 0.1 to 1000 poise. The viscosities of the fluids are measured using a rotary viscometer (Cole Palmer). All of the above fluids and fluid mixtures are Newtonian. The interfacial tension of the drop fluids is estimated from: (i) drop deformation experiments using small deformation theory (Taylor 1934), (ii) initial capillary wave deformation of a stationary liquid thread using linear theory (Tomotika 1935) and (iii) deformation and breakup of a stationary liquid thread studied using the boundary integral technique (see table 1). The details of method (iii) will be described elsewhere (Tjahjadi, Stone & Ottino 1992).

The experiment is started by using a pipette to inject a drop, with radius approximately 0.3 cm, about 5 cm below the surface of the bulk fluid. A stereomicroscope (Olympus SZ60) mounted to a Nikon N2000 camera body is

Drop fluids†	$p = \mu_i/\mu_e$‡	σ_1	σ_2	σ_3‖
$0.90A+0.10B$‖	2.8	9.1	10.5	11.0
$0.78A+0.22B$	1.0	n/a	10.7	11.3
$0.67A+0.33B$	0.40	9.5	11.1	11.9
$0.50A+0.50B$	0.067	10.1	11.5	12.7
$0.33A+0.67B$	0.010	10.4	11.8	13.0

† Volume fraction: A = no. 40 oil, B = l-bromonaphthalene.

‡ $T = 23\pm0.1$ °C, μ_e (23 °C) = 32.6 poise.

‖ σ_1, σ_2 and σ_3 are fluid–fluid interfacial tensions (dyne/cm) obtained from small deformation theory, linear stability theory, and boundary integral computations, respectively.

TABLE 1. Properties of fluid systems used

positioned normal to the cylinder about 9 cm from the drop. The objective lens of the stereomicroscope is equipped with a microscale allowing measurement with an accuracy ±5 μm. Illumination is provided by means of a fibre optic system (Olympus TV-S002 and TV-G001) that produces negligible heating effects. Drop deformation is generated by rotating the cylinders in opposite directions with a shear rate high enough to exceed the critical capillary number necessary for continuous drop extension. This procedure stretches the drop into a long fluid filament, typically 50–100 times the initial drop radius. The speeds of the cylinders are adjusted manually so that the centre of mass of the drop is positioned in front of the stereomicroscope.

Perturbations on the surface of the filament are suppressed during the extension. However, small-amplitude perturbations start to grow visibly after the motion is stopped. Based upon linear stability theory, there is one wavenumber, $x_{\text{opt}} = 2\pi a_m/\lambda$ (where a_m is the filament's mean radius and λ is the wavelength), which corresponds to the maximum rate of growth. However, in the experiments, a slight variation in the filament radius, or some other external perturbation, often leads to (axial) asymmetric amplification of disturbances. Consequently, along the filament there is more than one surviving wavenumber, generally confined to within $x_{\text{opt}} \pm 0.1$, with each wavenumber characterized by a slightly different growth rate. Also, of course, the local interface disturbance is actually a superposition of multiple wavenumbers, though it is a very good approximation to represent the initial small amplitude disturbance with a single wavenumber (for example, see figure 1).

Experiments are recorded photographically using Kodak Tmax b/w film. The unperturbed radius of the filament and the radii of the satellite drops are measured directly from the stereomicroscope; however, the amplitude of the filament during the evolution is measured from enlarged prints. The time evolution is recorded by means of a video recorder (with Dage-MTI 65 camera, video timer, and Olympus SZ-CTV C-Mount adapter) and a stopwatch is used to record the time of the first and the last pinch-off.

3. Numerical procedure

Consider a thread of a neutrally buoyant Newtonian liquid with undeformed radius a_m and viscosity μ_i, suspended in a bath of a second Newtonian fluid with viscosity μ_e. The viscosity ratio is denoted as $p = \mu_i/\mu_e$ and the interfacial tension between the two fluids is σ. We assume that σ is constant and any effects due to the

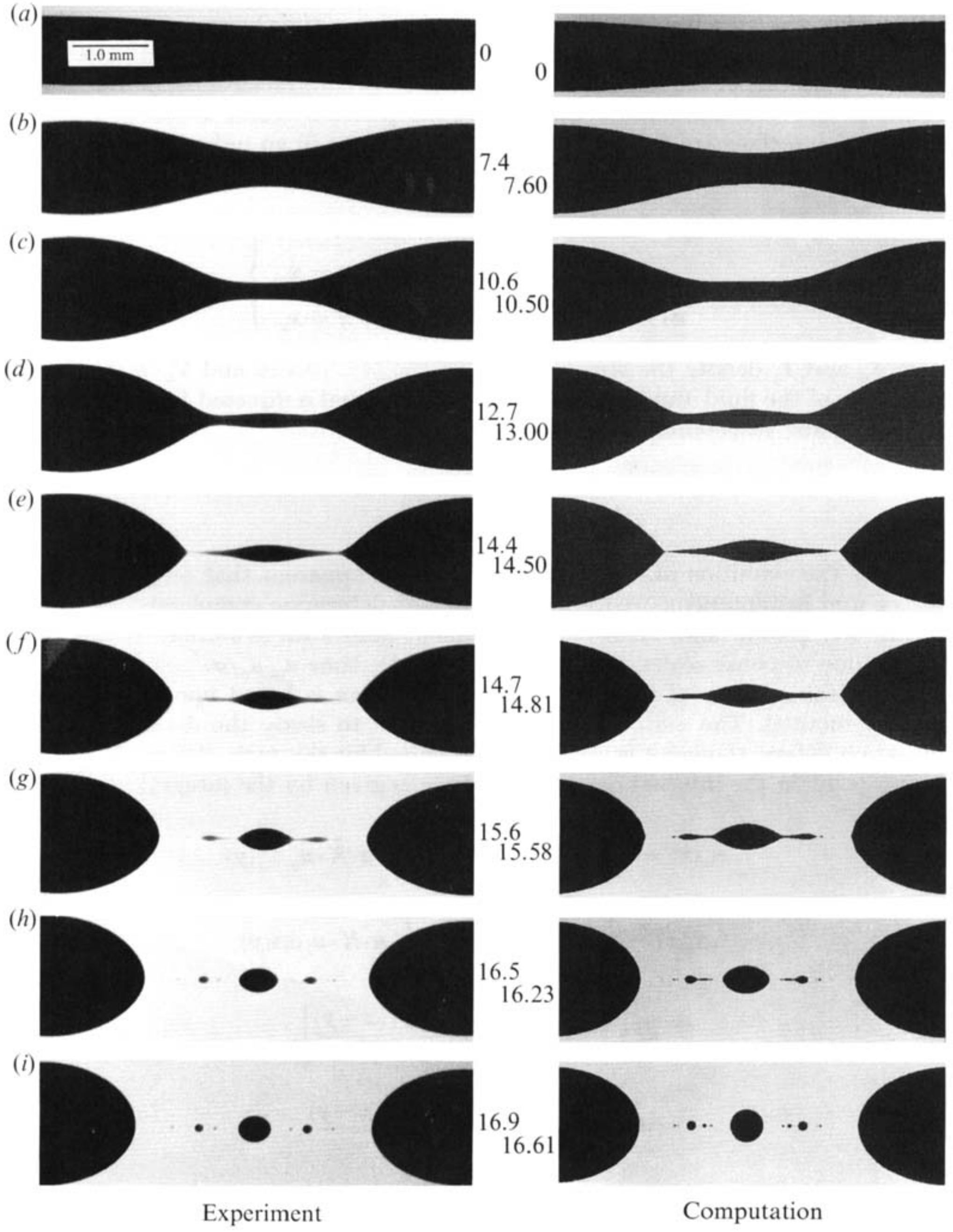

FIGURE 1. Time evolution leading to multiple pinch-offs of a segment of a highly extended fluid filament. The left-hand column shows the experimental results; the right-hand column the computational simulation. The viscosity ratio and wavenumber are 0.067 and 0.50 respectively. The dimensionless times shown correspond to experiment (top) and computation (bottom).

presence of surfactants are neglected. If inertial effects are small relative to viscous effects the evolution of the filament is described by Stokes equations in each fluid phase,

$$\left.\begin{aligned} \nabla^2 \boldsymbol{u}_i &= \nabla P_i, \quad \nabla\cdot\boldsymbol{u}_i = 0 \text{ (filament)},\\ \nabla^2 \boldsymbol{u}_e &= \nabla P_e, \quad \nabla\cdot\boldsymbol{u}_e = 0 \text{ (surrounding fluid)}.\end{aligned}\right\} \qquad (1)$$

Here all lengths have been non-dimensionalized by a_m, time by $a_m \mu_e/\sigma$, pressures by σ/a_m in the internal phase, and by $p\sigma/a_m$ in the external phase, and velocities by σ/μ_e. This scaling of the velocity is characteristic of interfacial-tension-driven flows. Points in the fluid domain are denoted by the position vector $\boldsymbol{x}$ and points at the fluid–fluid interface are denoted by $\boldsymbol{x}_s$. For a filament in an unbounded suspending fluid which is at rest, the boundary conditions are

$$\left.\begin{aligned} \boldsymbol{u}_e(\boldsymbol{x}) &\rightarrow 0 && \text{as } |\boldsymbol{x}| \rightarrow \infty, \\ \boldsymbol{u}_e &= \boldsymbol{u}_i && \text{for } \boldsymbol{x} = \boldsymbol{x}_s, \\ \boldsymbol{n}\cdot\boldsymbol{T}_e - \mathrm{p}\boldsymbol{n}\cdot\boldsymbol{T}_i &= \boldsymbol{n}(\boldsymbol{\nabla}_s\cdot\boldsymbol{n}) && \text{for } \boldsymbol{x} = \boldsymbol{x}_s. \end{aligned}\right\} \tag{2}$$

Here $\boldsymbol{T}_e$ and $\boldsymbol{T}_i$ denote the stress tensors in the two phases and $\boldsymbol{\nabla}_s\cdot\boldsymbol{n}$ is the mean curvature of the fluid–fluid interface with local normal $\boldsymbol{n}$ directed from the filament phase into the suspending phase. The kinematic condition,

$$\frac{\mathrm{d}\boldsymbol{x}_s}{\mathrm{d}t} = \boldsymbol{n}(\boldsymbol{u}\cdot\boldsymbol{n}), \tag{3}$$

describes the evolution of the drop interface. It is apparent that only the viscosity ratio p and instantaneous shape of the filament determine completely the velocity field at any instant and, hence, the subsequent interfacial evolution. However, the actual time response scales with the characteristic time $a_m \mu_e/\sigma$.

Numerical solution of this free-boundary problem is based upon the boundary integral method. The method has not been used to study the details of satellite formation before, though it is clearly ideally suited for this task. Briefly, the velocity at any point in the internal or external phase is given by the integral identities

$$\boldsymbol{u}_e(\boldsymbol{x}) = -\int_S \boldsymbol{n}\cdot\boldsymbol{T}_e\cdot\boldsymbol{J}\,\mathrm{d}S(\boldsymbol{y}) + \int_S \boldsymbol{n}\cdot\boldsymbol{K}\cdot\boldsymbol{u}_e\,\mathrm{d}S(\boldsymbol{y}), \tag{4}$$

$$\boldsymbol{u}_i(\boldsymbol{x}) = \int_S \boldsymbol{n}\cdot\boldsymbol{T}_i\cdot\boldsymbol{J}\,\mathrm{d}S(\boldsymbol{y}) - \int_S \boldsymbol{n}\cdot\boldsymbol{K}\cdot\boldsymbol{u}_i\,\mathrm{d}S(\boldsymbol{y}), \tag{5}$$

where
$$\boldsymbol{J} = \frac{1}{8\pi}\left[\frac{\boldsymbol{I}}{|\boldsymbol{x}-\boldsymbol{y}|} + \frac{(\boldsymbol{x}-\boldsymbol{y})(\boldsymbol{x}-\boldsymbol{y})}{|\boldsymbol{x}-\boldsymbol{y}|^3}\right],$$

$$\boldsymbol{K} = -\frac{3}{4\pi}\frac{(\boldsymbol{x}-\boldsymbol{y})(\boldsymbol{x}-\boldsymbol{y})(\boldsymbol{x}-\boldsymbol{y})}{|\boldsymbol{x}-\boldsymbol{y}|^5}.$$

In these equations, S represents the interface between the fluids and $\boldsymbol{y}$ is the integration variable. Taking the limit $\boldsymbol{x}\rightarrow\boldsymbol{x}_s$ and making use of the interfacial conditions (2), (4) and (5), generates an integral equation of the second kind for the interfacial velocity $\boldsymbol{u}_s(\boldsymbol{x}_s)$ (Rallison & Acrivos 1978):

$$\tfrac{1}{2}(1+p)\,\boldsymbol{u}_s(\boldsymbol{x}_s) + (1-p)\int_S \boldsymbol{n}\cdot\boldsymbol{K}\cdot\boldsymbol{u}_s\,\mathrm{d}S(\boldsymbol{y}) = -\int_S \boldsymbol{n}\cdot\boldsymbol{J}(\boldsymbol{\nabla}_s\cdot\boldsymbol{n})\,\mathrm{d}S(\boldsymbol{y}). \tag{6}$$

Since the thread is assumed to be axisymmetric, the azimuthal (θ) integration can be performed analytically and the surface integrals in (6) reduce to line integrals. The line integrals are solved numerically in a manner similar to that described in Lee &

Leal (1982) and Stone & Leal (1989); a few details regarding aspects specific to the implementation of the computations reported here are given in the Appendix. In particular, special care has been taken in order to resolve regions of high curvature while following the breakup process through several generations of satellite drops.

4. Results

4.1. *Satellite formation by multiple pinch-offs: a typical case*

In order to provide a setting for the presentation of experimental and numerical results, we consider a typical deformation and breakup experiment leading to multiple pinch-offs. This experiment, denoted as experiment A, is presented in the left column of figure 1. The viscosity ratio is 0.067 and the results that follow are representative of a large number of repeated experiments. Figure 1(*a*) shows a segment of a filament approximately from $\xi = 0$ to $\xi = 2\pi$ where ξ denotes a convenient dimensionless axial distance. The unperturbed radius of the filament is about 0.4 mm. The wavenumber for the segment shown is $x \approx 0.50$ and the dimensionless time t is shown next to each figure (top). The characteristic time of the experiment is $a_m \mu_e / \sigma = 0.9$ *s*. From the experimental data one can estimate that the largest fluid velocities (in the neighbourhood of the pinch-off location) are about 0.1 cm/s which yields a conservative estimate for a maximum Reynolds number of 10^{-3}; hence the dynamics are in the Stokes flow regime.

Initially, when the disturbances on the surface of the thread are relatively small, they take the form of a sinusoidal wave (see figure 1*a*, *b*) of a single wavelength. The maximum and minimum amplitude of the disturbances, denoted $A_{\max}$ and $A_{\min}$ respectively (see figure 3 for schematic representation), grow at the same rate and their magnitude during the initial stages of the process can be computed by means of linear stability theory. The linear theory predicts that breakup occurs at the midpoint $\xi = \pi$ when the minimum amplitude $A_{\min}$ is equal to the unperturbed radius of the filament. However, such a scenario is not attained; the interfacial-tension-driven motion becomes highly nonlinear as the curvature gradient develops, which leads to the formation of a slender tube around the trough part of the wave (see figure 1*c*). The ends of the slender tube are connected to the large mother drops originating from the crest parts of the wave.

Figure 1(*d*) shows that the motion at the middle of the central tube has now reversed its direction and the thread radius in this central region grows. This leads to the formation of the largest satellite drop. However, the ends of the tube, which are connected to the mother drop regions continue to contract. Thus, there are now three bulbous parts along the segment, two large ones at the ends and a smaller one at the centre. We see that very slender tubes bridging the two bulbous fluid regions are formed quickly, and the first pinch-off occurs. It should be pointed out that as it is impossible to start with a filament with a perfectly uniform radius and symmetric initial perturbation, the first pinch-offs almost never occur simultaneously. However, all the experimental results presented here are such that the time difference between the first pinch-offs is negligible. This is, of course, not true if the perturbation is asymmetric; in general, only 5–10 out of 100 experiments lead to nearly simultaneous first pinch-offs.

After the first pinch-offs, the fluid segment is divided into three parts, two mother drops at the ends and a centre drop which, depending on the viscosity ratio, may evolve into one or more satellite droplets (see figure 1*f*). The mother drop, immediately after the pinch-off, has a shape with a pointed end; this end quickly

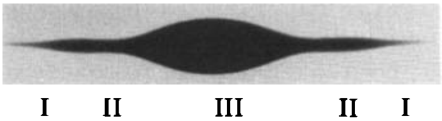

FIGURE 2. Definition of the regions of the centre drop.

retracts and becomes smooth as the drop relaxes back to a sphere. On the other hand, the centre drop undergoes several stages of shape change and possibly further breakups. In order to provide a setting for the remainder of the discussion we divide the centre drop into three parts, labelled I, II, and III, as shown in figure 2.

Let us now focus on the central region which undergoes multiple breakup (figure 1*f*–*i*). Figure 1(*g*) shows that there are two competing interfacial-tension-driven motions in regions II and III. The axial motion pushes the fluid towards the centre of the drop, and hence prevents further breakup. The radial motion causes the fluid interface to either expand or contract, forming a wavy surface that may undergo further breakup. It is apparent that in the experiment shown in figure 1(*g*) the axial motion does not overcome the radial motion; the interface in regions II and III undulate and fragment.

Qualitatively, the interfacial-driven dynamics during the continuous retraction and fragmentation are as follows: Initially the slender tubes in regions II and III start to swell owing to axial flow inward; the tube with the smaller radius grows at a faster speed. As a result the fluid in region III quickly forms a bulbous end. This end is connected by a very thin tube to region II of the drop which has grown into a relatively big bulb. The bulbous end and its thin connector undergo several stages of pinch-off producing several satellite droplets (see figure 1*h*). After region III is detached from the main body of the central region, region II forms a bulbous end, and again, is connected via a thin tube to region I. The mechanism that leads to the breakup is similar to that experienced previously by the fluid in region III. Figure 1(*g*, *h*) shows that the breakup in region II is initiated by the pinch-off at the joint between the thin tube and region I of the drop. In the end there are at least three visible droplets created in region III and four in region II. The total number of visible satellite and subsatellite droplets is 15 (see figure 1*i*). The radius of the smallest visible satellite is about 10 μm.

4.2. *Comparison of experiments with numerical studies*

Here we present a numerical investigation of experiment A described in §4.1. Notice that in the simulation we assume an 'infinite' axisymmetric fluid filament with only one initial wavenumber; however, as we have seen in experiments, such a condition is rarely satisfied as wavenumber variations occur along the entire length of the drop. In order to provide a one-to-one comparison, we match the initial condition in the computation with the one observed in the experiment, which is clearly approximated very well, for small initial disturbance amplitudes, by a single wavenumber. As long as the filament is mirror-symmetric, the uniform single wavenumber assumption appears to be reasonable. The calculation is continued through several generations of satellite drops, with breakup being modelled by touching of the interfaces, as discussed in the Appendix.

Figure 1 (right column) shows the evolution of a filament with the same initial condition as experiment A (i.e. $p = 0.067$, $x = 0.50$). The organization is such that parts $(a, b, \ldots)$ of the right column can be compared directly with parts $(a, b, \ldots)$ of the left column. The correspondence between experiment and computation up to the

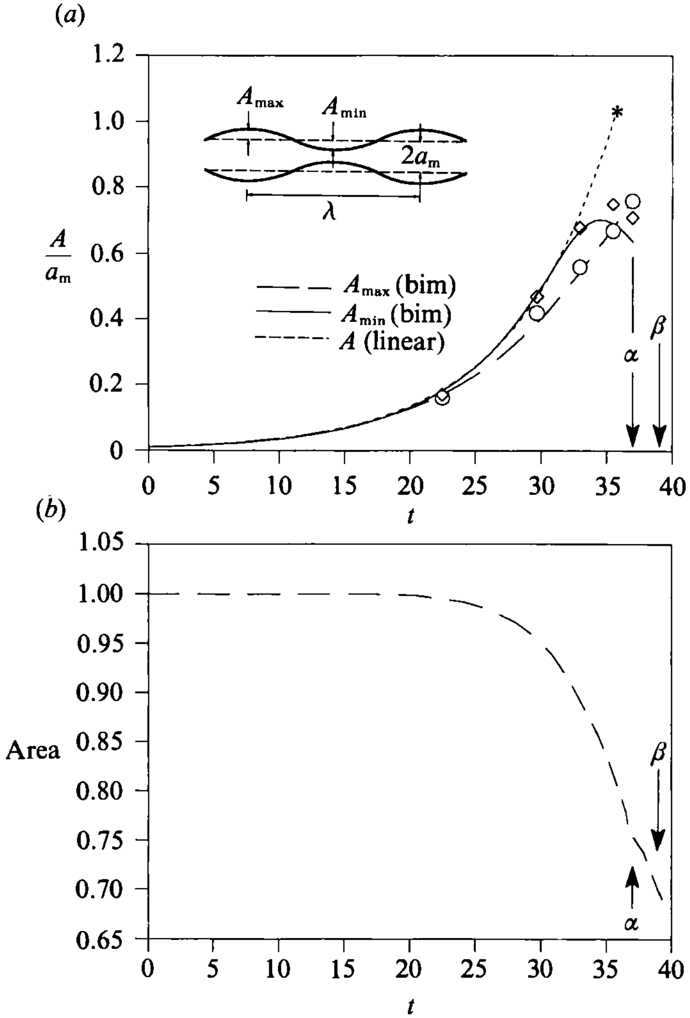

FIGURE 3. (*a*) The evolution of the amplitude A at $\xi = 0$ and π as a function of time obtained via the boundary integral method and linear stability theory. The parameters are the same as in figure 1. The maximum amplitude (at $\xi = 0$) is denoted $A_{\max}$, and minimum amplitude (at $\xi = \pi$) $A_{\min}$ (see inset). In linear theory $A_{\max} = A_{\min}$. Circles ($A_{\max}$) and diamonds ($A_{\min}$) are experimental data corresponding to figure 1. The asterisk (*) indicates the time of breakup based on the linear theory; (α) and (β) indicate the time of the first pinch-off, and the final pinch-off respectively. (*b*) The evolution of the surface area from $\xi = 0$ to 2π as a function of time obtained via the boundary integral method. All parameters correspond to part (*a*).

birth of the last visible satellite drop is good; in fact, the only way to tell them apart is by the slight unavoidable asymmetry in the experimental results.

Figure 3(*a*) shows the evolution of the amplitude of waves on the filament based on both the boundary integral simulation and linear stability theory. Denote the amplitude A at $\xi = 0$ as $A_{\max}$ and at $\xi = \pi$ as $A_{\min}$: the condition $A_{\max} = A_{\min} = 0$ corresponds to the unperturbed filament with radius a_m (see insert in figure 3*a*). As the initial condition for the computation we pick a relatively small initial perturbation, $A/a_m = 0.01$ (where A is either $A_{\max}$ or $A_{\min}$). During the initial stages of deformation, when A/a_m is small (< 0.15), both $A_{\max}$ (big dashed line) and $A_{\min}$ (solid line) coincide and grow at a relatively slow rate. However, as the perturbation

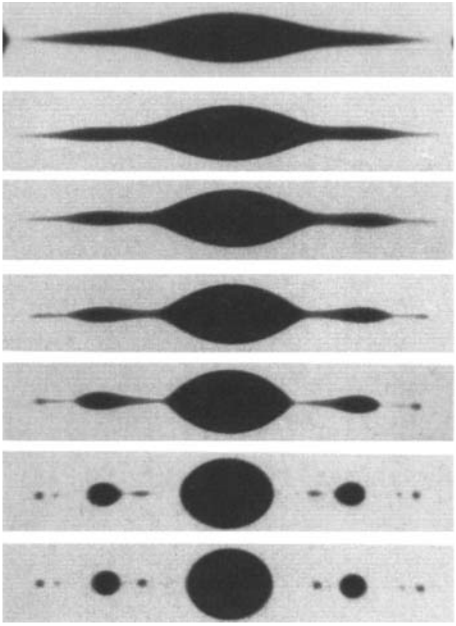

FIGURE 4. Experimental results showing a close-up of the time-evolution (top to bottom) of the centre region ($p = 0.067$, initial $x = 0.45$). Top, shape during the first pinch-off; bottom, shape after the last pinch-off.

becomes larger ($A/a_\mathrm{m} > 0.15$) A_min grows at a slightly faster rate than A_max. The growth slows down as the thin tube (or neck) forms around the central part of the filament. Eventually the growth rate of A_min reaches zero and then becomes negative as the centre of the slender tube starts to swell. On the other hand A_max increases exponentially until the first pinch-off occurs. The symbols, diamonds and circles, correspond to the photographs in figure 1(*a–e*) (left column) and represent A_min and A_max, respectively. The small dashed line is the calculation obtained based on the linear stability theory. The correspondence between the linear theory and the boundary integral simulation is reasonably good when A/a_m is less than 0.20. However, in the end the linear theory fails to capture the multiple pinch-offs shown in figure 1(*e–i*). Several of these features were indicated by Stone & Leal (1989) in a study of breakup of finite length fluid threads. Figure 3(*b*) shows the numerically calculated evolution of the filament surface area (for one wavelength) corresponding to the case presented in figure 3(*a*). Despite the constantly growing amplitude, the surface area does not change much for A/a_m less than 0.40. Finally, when breakup is complete, the area is reduced by more than 30%.

The first stage of the boundary integral simulation is terminated at the first pinch-off (numerically pinch-off is assumed to occur when the radius of the interface r is less than 10^{-3}). Then the second stage of the simulation is started, in which case the integration includes only the centre drop with its adjacent two mother drops (see Appendix for details). Figure 4 shows a blow-up of an experiment illustrating the evolution of the centre drop immediately after the first pinch-off (the viscosity ratio p is 0.067 and wavenumber x is 0.45). Figure 5 shows the corresponding computation with particular attention given to the details of the breakup process; the agreement is good. The 'pointed' tip of the drop (see arrow i) retracts towards the centre relatively quickly, thus transforming the end into a bulbous shape which is

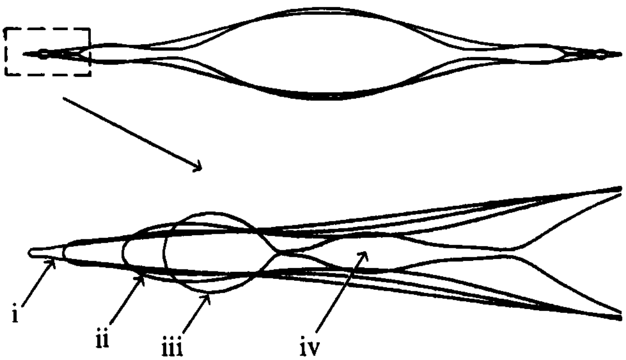

FIGURE 5. Computational results corresponding to figure 4. The top part shows the evolution of regions I–III. The bottom part shows a blow-up of the evolution of region III.

connected via a thin neck to the centre of the drop (see arrow ii). The neck continues to shrink radially, but reverses its direction as it reaches some critical radius, and starts to swell (this motion is qualitatively similar to the one shown in figure 1*c*–*e*). The fat neck (see arrow iv) is bridged to the bulbous tip (arrow iii) and the centre of the drop by means of very thin tubes. Then the bulbous tip pinches off from the neck, and the neck (arrow iv) pinches off from the main body. The pinch-off location is somewhere along the very thin tube and depending on the shape of the tube it may have more than one pinching location and therefore may result in the formation of one or more subsatellites. The presence of small satellites owing to previous breakup processes are neglected in the later stages of the computation which only studies the evolution of isolated threads surrounded by the two neighbouring mother drops. The evolution of region II of the centre drop is qualitatively similar to the evolution of region III, i.e. the end becomes bulbous, then pinches off, often producing several subsatellites.

The interfacial-tension driven process described above reveals self-repeating features. Breakup is always associated with the formation of a bulbous shape connected to another bulbous shape via a thin thread or a neck. Depending on the viscosity ratio and length, the neck undulates owing to capillarity and forms one or more bulbous shapes which are connected to one another via much thinner necks. The time evolution of the repetitive pinch-offs as well as the self-repeating nature of the breakup dynamics is illustrated in figure 6. The left-hand side of the figure corresponds to $\xi = 0$; the right-hand side to $\xi = 2\pi$. Unbroken drop phase corresponds to black and the bulk phase to white. The parameters are the same as in experiment A. The top of the figure corresponds to the filament prior to the first pinch-off (figure 1*e*) and the bottom to the fragments shortly after the final pinch-off (figure 1*i*). The evolution of the white (or black) boundaries corresponds to the boundaries of the drop fragments along the axial direction ($r = 0$). Figure 6 suggests self-similarity, i.e. invariance with respect to change of scale in the satellite generation process; relatively close upper and lower cutoffs, however, preclude the determination of a fractal dimension.

4.3. *Effects of viscosity ratio and wavenumber*

Experimental studies and numerical simulations are conducted over a range of viscosity ratios, $p = 0.010$, 0.067, 0.40, 1.0, and 2.8. The results are organized as follows: figures 7 and 8 show a comparison of experiments and computations

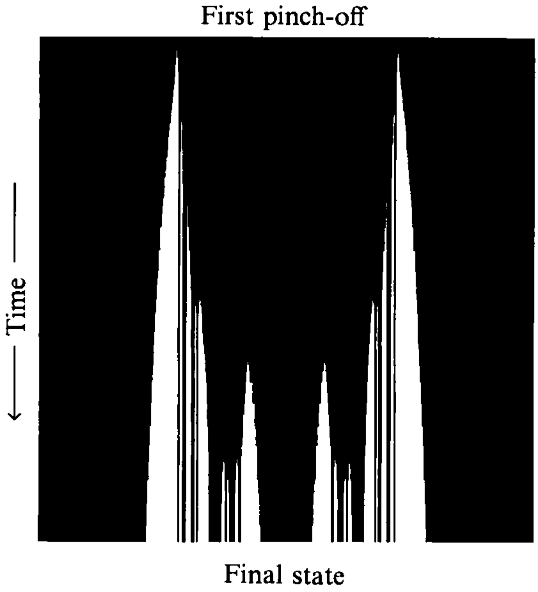

FIGURE 6. Time evolution (linear, top to bottom) of the boundaries of fragments at $r = 0$ from $\xi = 0$ to $\xi = 2\pi$. The drop phase is marked with black and the external fluid with white. The parameters are the same as in figure 1. The top corresponds to the filament just prior to the first pinch-off (figure 2*e*). indicated approximately by α in figure 3, and the bottom to the drop fragments shortly after the final pinch-off (figure 2*i*), indicated approximately by β in figure 3.

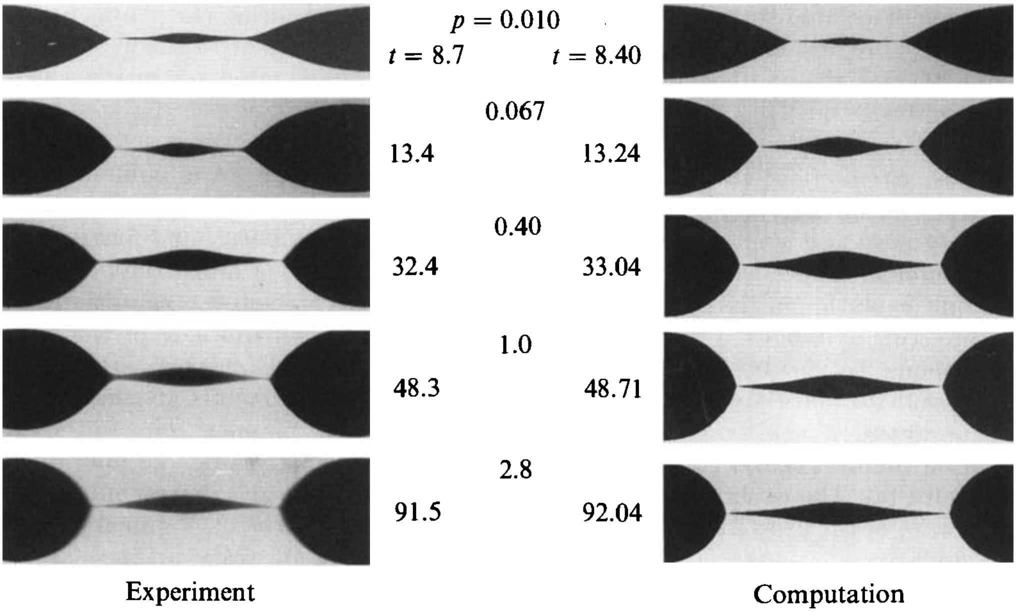

FIGURE 7. Shape of the filament before the first pinch-off; the left-hand column shows the experimental results, the right-hand column the computational simulation. Numbers next to the figures indicate the viscosity ratio (top) and dimensionless times (experiment middle, computation bottom).

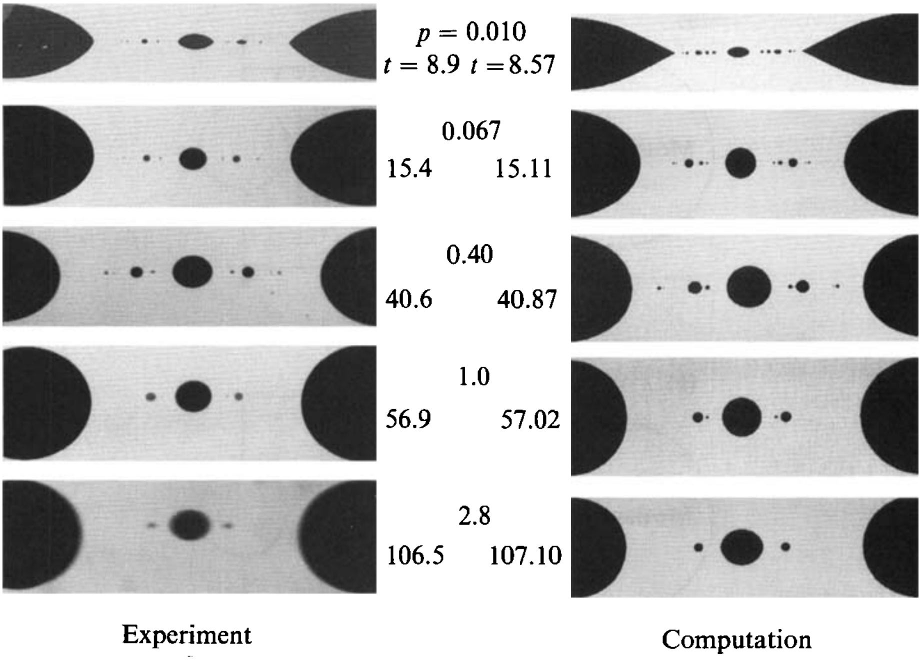

FIGURE 8. Shape of the filament after the last pinch-off; the left-hand column shows the experimental results, the right-hand column the computational simulation. Numbers next to the figures indicate the viscosity ratio (top) and dimensionless times (experiment middle, computation bottom).

corresponding to the first and last pinch-off, respectively. Figure 9 introduces a drop-labelling scheme used in the remainder of the discussion and figure 10 presents a catalogue of computational results for the final drop size distribution as a function of viscosity ratio and initial wavenumber. A quantitative summary of the results is presented in figures 11 and 12.

The effect of viscosity ratio is illustrated in figure 7 which shows photographs of experiments, just before the first pinch-off, alongside the corresponding computational results. Both experiments and computations indicate that the filaments exhibit different shapes as a function of viscosity ratio as the first pinch-off occurs, which lead to substantial differences in volume of the largest satellite drop. Slender mother drops with 'pointed' ends and slender I-regions are characteristic of low p; mother drops with somewhat more rounded ends and thicker I-regions are characteristic of high p. The evolution of the centre drop – regions I–III in figure 2 – depends strongly on viscosity ratio and qualitatively may be understood by noting that higher internal viscosities damp the flow processes which lead to thinning of the central region.

Figure 8 shows the state of the filament, $0 < \xi < 2\pi$, immediately after the last pinch-off. Inspection of many experiments shows that the number of visible satellite drops ranges from 3 ($p = 2.8$) to 19 ($p = 0.01$). The size of the smallest observable drop is approximately 10 μm. The largest drops present in figure 8 are still retracting back to a spherical shape. (See also figure 6. The amount of time it takes until the drops come to rest depends on the shape and the characteristic velocity for the interfacial-tension-driven shape changes, $u_\sigma = \sigma/\mu_e(1+p)$.) The size and spacing between satellite drops in equilibrium depends on the viscosity ratio p and, to a lesser extent, on the initial wavenumber of the disturbance. For low-viscosity-ratio

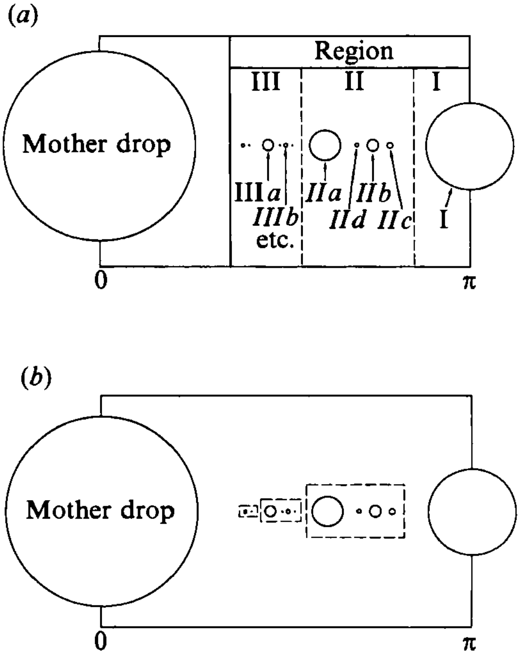

FIGURE 9. Top, labelling of satellites based on birth region and size; bottom, self-similarity of drop sizes.

systems, $p < O(0.1)$, the slender centre drop undulates and pinches off at many locations, thus giving birth to a string of small satellite drops. In fact, for the lowest p ($= 0.01$) the 'pointed' ends of both mother and centre drops are so 'unstable' that they form tiny droplets during the initial retraction. In the case of higher viscosity ratio systems, $p > O(1.0)$, the internal flows leading to breakup are damped and this results in the formation of fewer satellite drops. The corresponding computational results match the experiments reasonably well except for the case with the smallest $p(= 0.01)$ where the numerical error is the highest. The experiment with $p = 0.01$ produces many small satellites with radii less than $O(10^{-2})$ of the initial radius of the filament. This value is within the bounds of the numerical error.

Figure 9(*a*) shows a general labelling scheme corresponding to a typical experiment with low viscosity ratio. The labelling of the satellites indicates region of birth (I, II and III) and size, (*a*) being the largest droplet in a given region, (*b*) the next largest and so on. The self-similar character of the drop distribution is apparent also (figure 9*b*). The drops of region II are similar to a subset of region III and those, in turn, to a set of the smallest drops detected in the experiment. Figure 10(*a–d*) summarizes computational results of the final states, for different initial wavenumbers, corresponding to 4 different viscosity ratios, $p = 0.067$, 0.40, 1.0, 2.8 (these figures correspond to the bottom part of time-evolution graphs as shown in figure 6). Corresponding to each viscosity ratio, figure 10(*a–d*), five different wavenumbers are presented (the dominant wavenumber observed in a typical experiment is generally found to fall within $x_{\mathrm{opt}} - 0.10 < x < x_{\mathrm{opt}} + 0.10$). The case with $p = 0.01$ was analysed as well but it is not presented owing to the relatively large numerical errors. Satellites generated in region I are underlined with one line, in region II with two lines, etc. In general, as the viscosity ratio increases there are fewer satellites owing to the viscous damping of the internal motions. However, the number of

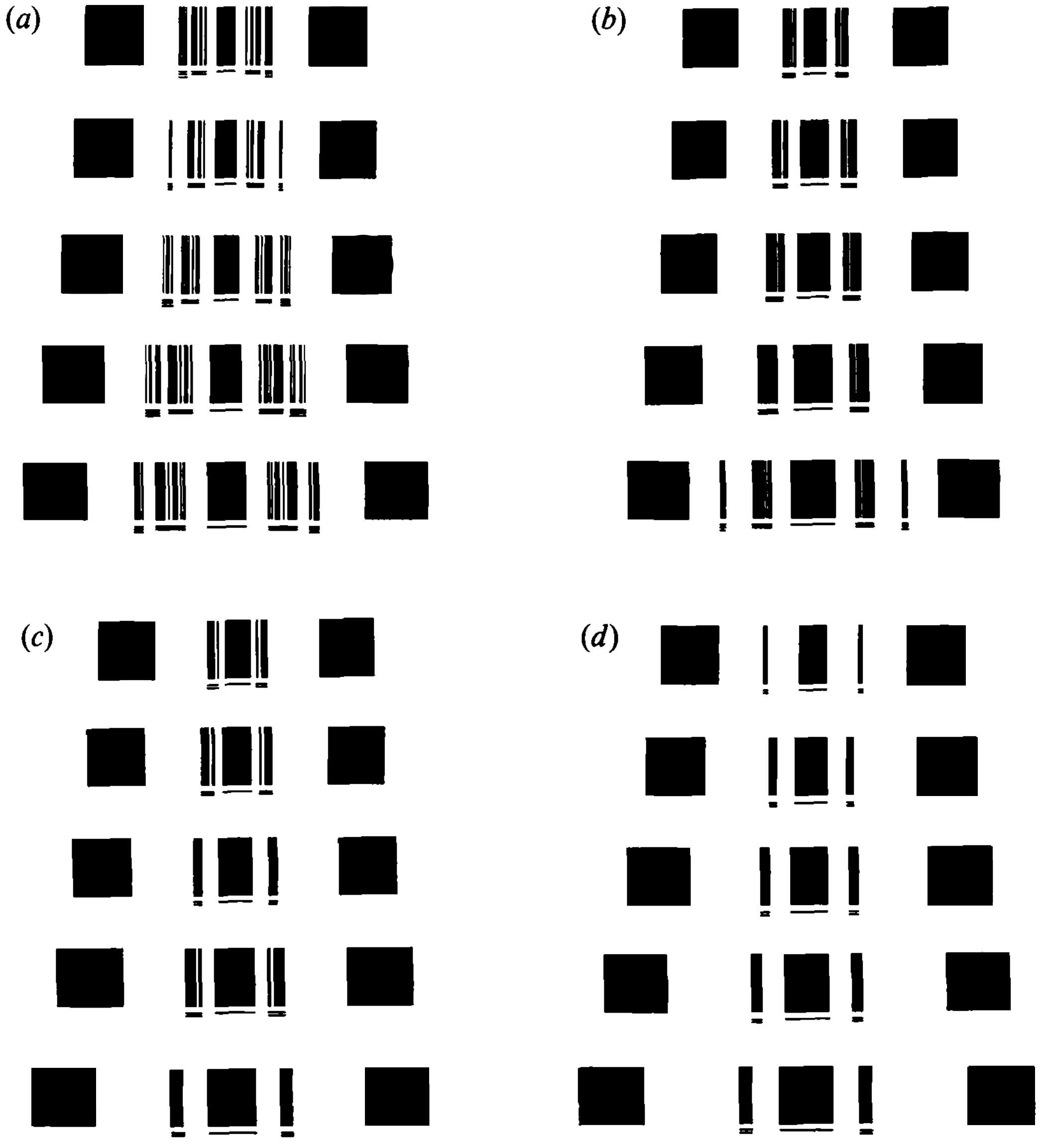

FIGURE 10. Equilibrium distribution of fragments from $\xi = 0$ to 2π as a function of viscosity ratio p and initial wavenumber x (in every case, top to bottom: $x_{\text{opt}}+0.10$, $x_{\text{opt}}+0.05$, x_{opt}, $x_{\text{opt}}-0.05$, $x_{\text{opt}}-0.10$. (*a*) $p = 0.067$, $x_{\text{opt}} = 0.55$; (*b*) $p = 0.40$, $x_{\text{opt}} = 0.59$; (*c*) $p = 1.0$, $x_{\text{opt}} = 0.56$; (*d*) $p = 2.8$, $x_{\text{opt}} = 0.50$.

satellites corresponding to a given p might vary according to the initial wavenumber (for example only three cases in figure 10(*c*) show the existence of drop II*b*). These small-scale features are often observed in the experiments but are difficult to repeat owing to small variations in the initial conditions. Large-scale features, such as more satellites at lower viscosity ratio, on the other hand, are always reproducible.

Figures 11 and 12 focus on equilibrium features and time-evolution, respectively. Figure 11 compares experimental and computational results in terms of the ratio of the radius of selected satellites relative to the radius of the mother drop. The drops considered are I, II*a*, and II*b* in figure 9(*a*). Experimental data show three families

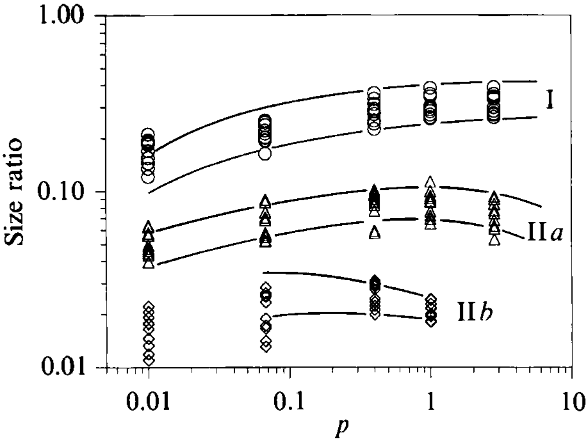

FIGURE 11. Size ratio between drop I, II*a*, and II*b* and mother drop as a function of viscosity ratio. Experimental results of various initial wavenumbers are plotted in symbols, bounded by two curves obtained from the computations. The upper curve corresponds to a computation with a wavenumber $x_{\text{opt}}-0.10$; the lower curve to $x_{\text{opt}}+0.10$.

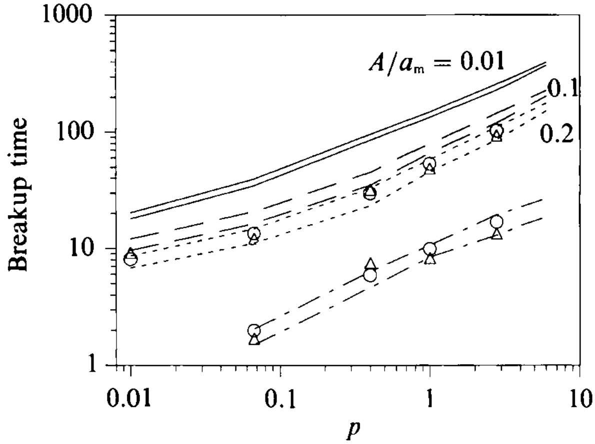

FIGURE 12. Length of time necessary for the filament to reach the first pinch-off with ——, initial amplitude $A/a_m = 0.01$; ——, 0.1; – – –, 0.2, as a function of viscosity ratio. ———, time difference between the first pinch-off and the final pinch-off. In all cases the upper curve corresponds to the computation with $x_{\text{opt}}-0.10$ and lower curve to $x_{\text{opt}}+0.10$. △, ○, data from two different experiments corresponding to initial amplitude $A/a_m \approx 0.2$.

of curves (indicated by symbols) bounded by two continuous curves corresponding to computations with initial wavenumber $x = x_{\text{opt}}-0.10$ (upper curve) and $x_{\text{opt}}+0.10$ (lower curve). The experimental data occupy a relatively wide band owing to different wavenumbers which characterize the initial state; however, we found that in general the radius ratio increases as the wave number decreases; this is in agreement with the computational predictions.

Figure 12 shows the length of time (non-dimensionalized with respect to $a_m \mu_e/\sigma$) necessary for the filament to reach the first pinch-off, as a function of the initial disturbance amplitude. Until now the computational results presented have been based on the premise that the initial perturbation is a relatively small sinusoidal amplitude $A/a_m = 0.01$. Clearly it is rather difficult to measure such a small amplitude in the experiments. Moreover the rate of growth of the amplitude, $\mathrm{d}A/\mathrm{d}t$, is initially rather small and large errors are likely. Therefore the experimental results are compared with computations after the amplitude has grown considerably, say $A/a_{\mathrm{m}} \approx 0.20$, and the rate of growth $\mathrm{d}A/\mathrm{d}t$ is larger. The computational results displayed in figure 12 correspond to three initial disturbance amplitudes, $A/a_{\mathrm{m}} =$ 0.01, 0.1 and 0.2. Also, shown in figure 12 is the time difference between the first pinch-off and the last pinch-off. The computations correspond to two initial wavenumbers, $x_{\mathrm{opt}}+0.1$ and $x_{\mathrm{opt}}-0.10$, which succeed in bounding the experimental results. It is apparent that once the first pinch-off occurs, all other breakups occur rather quickly. For example for $p = 1$, it takes over 10^2 time units to reach the first pinch-off but only $O(1)$ units to complete the breakup process. These results can be used to estimate the interfacial tension and viscosity ratio.

5. Conclusions

In this paper we have documented the shape evolution and eventual breakup of a highly extended fluid filament completely immersed in a second immiscible fluid. The deformation and breakup processes are studied numerically and the experimental results presented are representative of a large number of repeated experiments. Satellite drops are generated owing to multiple breakup sequences around the neck region of a highly deformed filament. For the fluid systems under investigation, $0.010 < p < 2.8$, the centre drop always experiences further breakups, generating 3 satellites at $p = 2.8$ up to 19 visible satellites at $p = 0.010$, where the smallest observable satellites are about 10 μm in radius. The number of satellite droplets and their relative sizes depend strongly on the viscosity ratio and are also influenced, though to a lesser extent, by the initial disturbance wavenumber. The dominant initial wavenumber, however, cannot be fixed in our experiments; it usually varies within 20% of the optimum value predicted by linear stability theory. On average, the sizes of the two largest satellites relative to their mother drop are bigger when $p > 0.4$ and the maximum occurs for $p \approx 1$. The breakup mechanism that leads to multiple satellite formation is self-repeating in the sense that every pinch-off is always associated with the formation of a neck, the neck undergoes an additional pinch-off, and the process repeats at smaller scales. Typically the resolution obtained in the computations is about an order of magnitude better than the experiments and in general the overall agreement between computations and experiments is very satisfactory. However, we could only follow a few cascades of 'neck-formation and pinch-off' before we are limited by either the optical resolution in the case of the experiments or the number of nodes in the case of computations.

The results presented here are relevant to the prediction of fragment sizes in mixing operations. More specifically, the quantitative results might be used in conjunction with recent studies involving stretching and folding of viscous filaments and stretching distribution in two-dimensional time periodic flows (Tjahjadi & Ottino 1991; Muzzio, Swanson & Ottino 1991) in order to obtain the drop size distribution produced upon drop fragmentation in complex chaotic flows. It has been established that the distribution of stretching within chaotic flows is self-similar (Muzzio, Swanson & Ottino 1991). There are clear indications that the drop-size distributions corresponding to a wide range of viscosity ratios are self-similar as well. Since the radii of the largest drops are, up to a multiplicative constant, inversely proportional to the length stretch, it therefore follows that distributions of mother drops are self-similar as well. It is in this context that the results obtained here prove useful: for each viscosity ratio, each mother drop carries a distribution of satellites quantified by figure 11. The superposition of all these curves should produce, to a first approximation, the entire drop size distributions reported by Muzzio *et al.* (1991).

This work was supported through a grant awarded to J.M.O. by the Department of Energy, Division of Basic Energy Sciences (DE-FG02-91ER14182). H.A.S. was supported by a PYI Award from the National Science Foundation.

Appendix

The numerical solution of the integral equation (6) for the interfacial velocity $\boldsymbol{u}_s$ has been described by earlier investigators. Because the focus of this research has been to understand the details of the breakup process, in particular the evolution of shape through the formation of several generation of satellite drops, some modifications were introduced and they are summarized in this Appendix.

The initial condition for the filament is given by a single wavenumber and the (small) amplitude of the dominant disturbance present on drops observed in the experiments. The initial shape is assumed to be symmetric with respect to planes passing through $\xi = \mathrm{i}\pi$ (where i is an integer) orthogonal to the axial (ξ) direction (see figure 13). This periodic shape is represented by the summation of repeating units, where each unit, denoted as M_i spans axial distances from $\xi = \mathrm{i}\pi$ to $\xi = (\mathrm{i}+1)\pi$ and the shape is represented by a number of collocation points N which subdivide the surface into smaller elements. The interfacial velocity is assumed to be uniform over each element. The integral equation is reduced to a system of linear algebraic equations by replacing the integrals with a sum over the elements describing the surface. In the vicinity of the singularity (i.e. $\boldsymbol{x}_s = \boldsymbol{y}$), where rapid variation of the integrand occurs, the element of interest is subdivided into three smaller sub-elements prior to numerical integration. A small region, typically 10^{-4}–10^{-5} the initial radius of the filament, is cut out around the singularity and the integration over the singular portion is performed analytically.

Since the geometry of the interface must be determined as part of the solution, and because the evolution equations involve curvature, hence second derivatives of the shape function, the drop shape must be represented accurately. An arclength parametrization method coupled with cubic splines is used to generate a smooth and accurate representation of the interface. For example, if s represents a measure of the arclength, the collocation points on the interface, labelled using cylindrical coordinates (r, z) are parametrized so that $r = r(s)$ and $z = z(s)$, where $z = \xi/x$, describe the filament's interface. Such a shape-fitting routine has been demonstrated to be accurate for describing highly distorted drop shapes and the long-time evolution of highly extended, though finite, fluid filaments (Stone & Leal 1989).

Finally, owing to axial periodicity, we only need to obtain the velocity profile along one representative unit (denoted by M_j) consisting of N elements. However, the integration is performed over lengths $2n$ (i.e. from $M_{\mathrm{j}-n}$ to $M_{\mathrm{j}+n}$) such that we still obtain an accurate velocity profile with a minimum amount of computing time. The truncation of the infinite periodic filament to a finite integration length is achieved by comparing the velocity profiles computed with different lengths n with the 'ideal' profile computed with a very large n, say $n = 100$. Based on the results computed at a few selected nodes on unit M_j, we then choose a value of n which yields the velocity profile within some tolerance of the $n = 100$ calculation. For typical runs, where

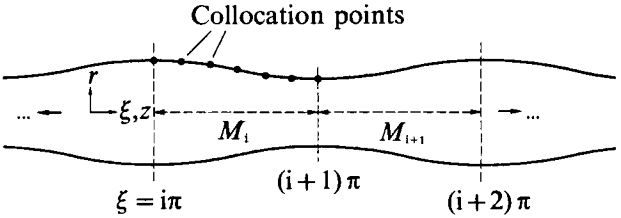

FIGURE 13. Definition of variables on a perturbed fluid filament.

$n = 20$, this tolerance is about $O(10^{-3})$ or smaller for $p > 0.06$ and about $O(10^{-2})$ for $p = 0.01$.

Some additional details of the implementation include evaluating all integrals using five-point Gauss quadrature and the interface shape is updated by solving the kinematic condition (equation (3)) using an explicit Euler method. For the case viscosity ratio $p \neq 1$, matrix inversion of the algebraic system resulting from the integral equations is accomplished by LU decomposition (Press *et al.* 1986). Also, the timestep ranges from 0.001 to 0.1 depending on the value of the viscosity ratio p and the magnitude of the largest velocity. For example, when $p > 1$ and the curvature $\nabla_s \cdot \boldsymbol{n}$ is small, we use a larger timestep since the resulting velocities are small.

The collocation points are evenly redistributed based upon arclength along the interface at every timestep. When a region of high curvature gradient begins to develop around the pinch-off region, more points are added in the high curvature locale in order to maintain the continuity of the curvature profile and accurate resolution of the filament shape. Also, the magnitude of the timestep is reduced since the velocities at the region of high curvature increase as the curvature magnifies. Such refining is done more than once (usually 5 times or more) prior to the first pinch-off. We assume that the first breakup occurs when the filament's radius drops below 10^{-3}. At this time, we typically have about 60–80 node points (within the unit M_j) representing the interface shape and the distance between collocation points in the vicinity of the highest curvature is smaller than 0.01, which is sufficient owing to the smooth surface representation generated by the splines.

All calculations are done in double precision. Typical c.p.u. times on a Sun Sparc station for one timestep are about 50 s for the case $N = 20$ and $n = 20$. As a check on the numerical calculations, the drop volume as well as the sum of $\boldsymbol{u}_s \cdot \boldsymbol{n}$ along the interface on M_j are monitored. For every iteration the sum of $\boldsymbol{u}_s \cdot \boldsymbol{n}$ is reasonably small [$O(10^{-3})$ or smaller for $p > 0.06$ and $O(10^{-2})$ for $p = 0.01$] and at the end of the simulation the overall volume changes are approximately 0.6, 0.6, 0.6, 2 and 10% of the original volume for $p = 2.8$, 1.0, 0.4, 0.067 and 0.01, respectively. Note that the highest errors correspond to the lowest viscosity ratios as previous researchers have observed.

Two numerical codes are written to simulate the filament before the first pinch-off and after the first pinch-off, respectively (see definition of first pinch-off in §4.1). The integration of (6) before the first pinch-off is done over 20 unit lengths, i.e. $n = 20$, whereas after the first pinch-off the integration is done only within one wavelength. For example, in order to compute the interfacial velocity profile of the centre drop (see §4.1), we only take into account the presence of the two adjacent mother drops. The effects of other droplets upon the centre drop are shielded by the presence of the relatively large, only slightly deformed, mother drops. Also, although mother drops are always accounted for, when the centre drop fragments, any satellites, which are relatively small and nearly spherical, are neglected when computing the evolution of any remaining centre filaments. Finally, we note that in the experiment, all breakup events generate shapes which appear initially to have pointed ends; however, magnification suggests that the ends are actually rounded (note that this observation is not made at the time of the pinch-off, but after some retraction, about 1–2% of the drop's length, has occurred). Based upon this observation the end conditions of the drop following a breakup event are still modelled as being rounded which simply amounts to setting the spline end condition as $\mathrm{d}z/\mathrm{d}s = 0$.

REFERENCES

BENTLEY, B. J. & LEAL, L. G. 1986 An experimental investigation of drop deformation and breakup in steady two-dimensional linear flows. *J. Fluid Mech.* **167**, 241–283.

BOGY, D. B. 1979 Drop formation in a circular liquid jet. *Ann. Rev. Fluid Mech.* **11**, 207–228.

CHAUDHARY, K. C. & MAXWORTHY, T. 1980*a* The nonlinear capillary instability of a liquid jet. Part 2. Experiments on jet behaviour before droplet formation. *J. Fluid Mech.* **96**, 275–286.

CHAUDHARY, K. C. & MAXWORTHY, T. 1980*b* The nonlinear capillary instability of a liquid jet. Part 3. Experiments on satellite drop formation and control. *J. Fluid Mech.* **96**, 287–297.

CHAUDHARY, K. C. & REDEKOPP, L. G. 1980 The nonlinear capillary instability of a liquid jet. Part 1. Theory. *J. Fluid Mech.* **96**, 257–274.

ELEMANS, P. H. M. 1989 Modeling of the processing of incompatible polymer blends. PhD thesis, Eindhoven Technical University, The Netherlands.

ELEMANS, P. H. M., JANSSEN, J. M. H. & MEIJER, H. E. H. 1990 The measurement of interfacial tension in polymer/polymer systems: the breaking thread method. *J. Rheol.* **34**, 1311–1325.

GOEDDE, E. F. & YUEN, M. C. 1970 Experiments on liquid jet instability. *J. Fluid Mech.* **40**, 495–511.

LEE, S. H. & LEAL, L. G. 1982 The motion of a sphere in the presence of a deformable interface. II. A numerical study of the translation of a sphere normal to an interface. *J. Colloid Interface Sci.* **87**, 81–106.

MANSOUR, N. & LUNDGREN. T. S. 1990 Satellite formation in capillary jet breakup. *Phys. Fluid* A **2**, 1141–1144.

MIKAMI, T., COX, R. & MASON, R. G. 1975 Breakup of extending liquid threads. *Intl J. Multiphase Flow* **2**, 113–118.

MUZZIO, F. J., SWANSON, P. D. & OTTINO, J. M. 1991 The statistics of stretching and stirring in chaotic flows. *Phys. Fluids* A **3**, 822–834.

MUZZIO, F. J., TJAHJADI, M. & OTTINO, J. M. 1991 Self-similar drop size distributions produced by breakup in chaotic flows. *Phys. Rev. Lett.* **67**, 54–57.

PRESS, W. H., FLANNERY, B. P., TEUKOLSKY, S. A. & VETTERLING, W. T. 1986 *Numerical Recipes*. Cambridge University Press.

RALLISON, J. M. & ACRIVOS, A. 1978 A numerical study of the deformation and burst of a viscous drop in an extensional flow. *J. Fluid Mech.* **89**, 191–209.

RAYLEIGH, LORD 1878 On the instability of jets. *Proc. Lond. Math. Soc.* **10**, 4–13.

RUMSCHEIDT, F. D. & MASON, S. G. 1962 Breakup of stationary liquid threads. *J. Colloid Sci.* **17**, 260–269.

SAX, J. E. & OTTINO, J. M. 1985 Influence of morphology on the transport properties of polystyrene/polybutadiene blends: experimental results. *Polymer* **26**, 1073–1080.

STONE, H. A. & LEAL, L. G. 1989 Relaxation and breakup of an initially extended drop in an otherwise quiescent fluid. *J. Fluid Mech.* **198**, 399–427.

TAYLOR, G. I. 1934 The formation of emulsions in definable fields of flow. *Proc. R. Soc. Lond.* A **146**, 501–523.

TJAHJADI, M. & OTTINO, J. M. 1991 Stretching and breakup of droplets in chaotic flows. *J. Fluid Mech.* **232**, 191–219.

TJAHJADI, M., STONE, H. A. & OTTINO, J. M. 1992 Estimating interfacial tension via breakup of highly extended fluid filaments and relaxation of moderately extended droplets. In preparation.

TOMOTIKA, S. 1935 On the stability of a cylindrical thread of a viscous liquid surrounded by another viscous fluid. *Proc. R. Soc. Lond.* A **150**, 322–337.

TOMOTIKA, S. 1936 Breakup of a drop of viscous liquid immersed in another viscous fluid which is extending at a uniform rate. *Proc. R. Soc. Lond.* A **153**, 302–318.